Vertical-Axis Wind Turbine Steady and Unsteady Aerodynamics for Curved Deforming Blades

Kevin R. Moore* and Brandon L. Ennis†

Sandia National Laboratories‡, Albuquerque, NM 87185

Vertical-axis wind turbines' simpler design and low center of gravity make them ideal for floating wind applications. However, efficient design optimization of floating systems requires fast and accurate models. Low-fidelity vertical-axis turbine aerodynamic models, including double multiple streamtube and actuator cylinder theory, were created during the 1980s. Commercial development of vertical-axis turbines all but ceased in the 1990s until around 2010 when interest resurged for floating applications. Despite the age of these models, the original assumptions (2-D, rigid, steady, straight-bladed) have not been revisited in full. When we apply the current low-fidelity formulations to modern turbines in the unsteady domain, we find aerodynamic load errors nearing 50%, consistent with prior literature. However, we identify a set of steady and unsteady modifications that remove the majority of error, limiting it near 5%. We show how to reformulate the steady models to allow for unsteady inputs including turbulence, deforming blades, and variable rotational speed. We also present a new unsteady approximation that increases numerical speed by 5-10x. Combined, these modifications enable full-turbine unsteady simulations with accuracy comparable to higher-fidelity vortex methods, but over 5000x faster.

I. Introduction

VERTICAL axis wind turbine (VAWT) aerodynamics are unique in that the blades pass through their own wake, capturing energy and inducing velocity in both the upstream and downstream areas (as depicted in Fig. 1). This requires the mutual influence of the upwind and downwind portions to be calculated for accurate predictions. Although vortex methods and computational fluid dynamics (CFD) do this very well, a faster method is needed to enable trade studies, fully coupled aerostructural analysis, and optimization. The need for a simplified aerodynamics model has led to many variations including streamtube [1], multiple streamtube [2, 3], double multiple streamtube (DMS) [4–6], and actuator cylinder (AC) theory [7]. DMS and AC are the primary models used, with AC being more preferred [8–10] due to its more physically accurate nature [11]. However, DMS is generally comparable and runs approximately 20x faster.
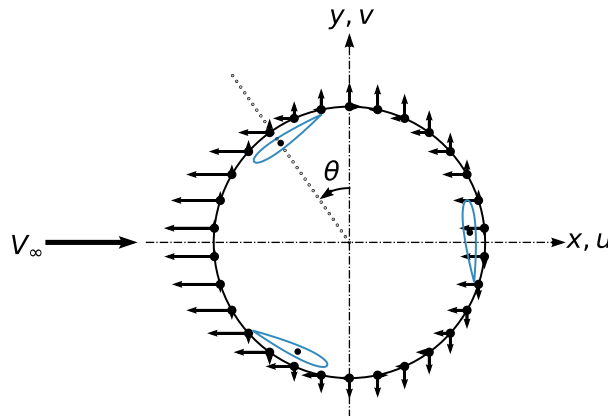

Fig. 1 VAWT 2-D horizontal slice with induced velocity u and v components depicted by arrows.

Both the DMS and AC formulations rely on blade element theory to predict blade loads, but use different wake-turbine interaction models. They were both originally derived for a 2-D steady-state infinite cylinder of unchanging radius. Although these simplifications have proven useful over the last four decades, they are not representative of a large VAWT with curved deforming blades. While it is possible that stacks of cylinders can be used to approximate 3-D curved blades [8, 12], this leads to significant errors at the blade level [13]. Though the general consensus seems to be that these errors are due to the neglect of 3-D effects, some authors have made partial progress at resolving the error [9, 12, 14–16, 16]. However, none have clearly and fully presented the modifications required and validated their work with comparisons of loads at the blade level.

This study is intended to set the stage for the future use and development of the DMS and AC models in a formulation that can accurately handle curved deforming blades for both steady and unsteady analysis. We limit our overview of the baseline models to only what is needed to understand the modifications and recommend readers interested in recreating the full baseline models review the original cited sources. This paper is structured into three major sections: Steady blade-element modifications, steady wake interaction modifications, and unsteady model improvements. Verification/validation is done at each stage, with the common baseline turbine being defined here, before the modifications are presented.

II. Baseline Turbine for Verification

Prior to discussing model modifications, the baseline verification/validation turbine geometry used for each case is defined. We use the Sandia National Laboratories (SNL) three-bladed 5 meter turbine [17], upgraded with full troposkein NACA-0015 blades [18]. This turbine was chosen for its simplicity, availability of performance data, and prior validation for the CACTUS free-wake vortex solver [19]. The turbine is 5 meters in diameter, has a height to diameter ratio of 1.02, a constant chord of 6 inches, and zero degrees installed twist, but a 40% chord mount point (which gives an effective aerodynamic twist that varies along the blade, see [20]). We model the SNL 5m with CACTUS, AC, and DMS using 31 vertical discretizations (making 30 slices). The CACTUS case models the turbine in full 3-D, while the AC and DMS cases use the stacked cylinder/slices approach (uncorrected and corrected based on this paper). The Boeing-Vertol [21] dynamic stall model is used and and 30 timesteps per revolution is the azimuthal discretization. The flow conditions are matched with the nominal test site parameters in Albuquerque, NM. The rotor rotation rate was held constant at 150 RPM. The curvature, local radius, and other required parameters are based on the nominal turbine parameters and troposkein shape. Figure 2 shows the turbine and troposkein shape. For CACTUS specifically, the wake cutoff parameter was set at 3 diameters, and the model was run until the change in coefficient of performance had converged below 1E-4.

III. Steady Blade-Element Modifications

A. Baseline Actuator Cylinder and Double Multiple Streamtube Blade-Element Theory

Blade elements are discrete portions along the blade path where lift, drag, and moment forces can be calculated or looked-up from airfoil polars based on input angle of attack and local velocity. Both the AC and DMS solve for the

Fig. 2   SNL 5m three-bladed turbine showing troposkein shape.

aerodynamic flow field (wake) subject to blade forces from the blade elements, but the blade forces depend on the flow field, meaning that there is no closed form solution. Iteration is required to find the solution where the blade and flow field interactions match. This is similar to blade element momentum theory [22] for horizontal-axis turbines/propellers, but different in that the blade-element forces are cross-ways to the flow as depicted in Fig. 1. The original DMS and AC models' blade elements were derived with respect to blade normal and tangential forces, but the infinite cylinder assumption led prior researchers to treat the normal vector as a radial vector, neglecting vertical velocity and force components, even for highly curved/sloped blades. A turbine with curved/sloped blades was therefore modeled with many slices resembling stacked cylinders as opposed to smooth and continuous slices.

B. Blade-Element Formulation Modifications

Even though the original model derivations use the term *normal*, they do not include cases where the normal vector differs from the radial vector. Solving for curved blades with only the radial component does not yield the same solution as solving with the true normal. Additionally, this effect cannot be captured by simply stacking an infinite number of cylinders due to the additional blade length error this causes.

Following standard right-hand rule notation, blade slope (δ) is defined from the vertical-axis by the arctangent of the change in x-direction divided by the change in z-direction. Blade slope is positive for the lower portions of the blade and negative for the upper. The normal vector $\hat{n}$ is perpendicular to the slope. Therefore the angle from the horizontal axis to the blade

Fig. 3 Force and velocity vectors transformed from radial to normal.

normal equals the blade slope angle as in Fig. 3. To convert from the radial to normal frame of reference is a simple trigonometric matter. However, due to the blade elements' frame of reference in the fluid domain (force on the fluid as opposed to force on the blade), blade slope affects forces and velocities differently.
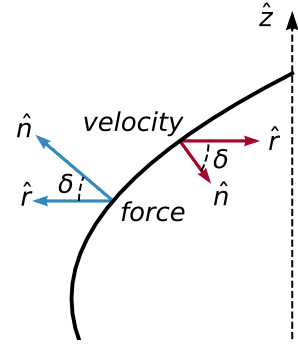
1. Blade Slope Effects on Velocity

Blade-element lift, drag, and moment force calculations require accurate local velocities. For the models of interest, radial velocity consists of freestream V_∞ and velocity induction factors u and v rotated by the turbine azimuthal angle θ as shown in the left portion of Eq. (1). However, since all of these components are planar, but normal (non-planar) velocity is needed, the planar components are corrected by cosine of the slope as shown in the right portion of Eq. (1). The tangential velocity needs no correction as it is perpendicular to blade slope.

$$
\begin{aligned}
V_n &= \left(V_\infty(1+u)\sin\theta - V_\infty(v)\cos\theta\right) * \overbrace{\cos\delta}^{\text{correction}} \\
V_t &= V_\infty(1+u)\cos\theta + V_\infty(v)\sin\theta + \Omega r
\end{aligned}
\tag{1}
$$

2. Blade Slope Effects on Force

Blade slope affects forces in two specific areas, namely the airfoil lift and drag coefficients' normalization and how the normal force is split between radial and vertical. First, in the blade-element formulations used by DMS and AC, once the local velocity vector is known, the airfoil 2-D lift and drag coefficients are calculated from airfoil polars. These coefficients are aligned with the local flow velocity, so they must be rotated back by the local inflow direction to get the local blade normal and tangential force coefficients c_n and c_t. However, these coefficients are *per unit span*. For a turbine slice of unit height, the sloped blades' span is not the same as the unit height, but is increased by multiplying by the secant of the blade slope. The modification required for the discrete normal volume force per height Q'_n used in the AC residual equation is shown in Eq. (2) (compare Ning [12] Eq. 30 and note that radial loading should now be termed normal loading). The modification for the DMS thrust force T'_h used in its residual equation is shown in Eq. (3) (compare Ayati [6] Eq. 11). Air density is ρ, local velocity magnitude is W, chord length is c, B is number of blades, and r is local radius. Both equations assume unit height.

$$
Q'_n = \left(\frac{Bc}{4\pi r} c_n \left(\frac{W}{V_\infty}\right)^2\right) * \overbrace{\sec\delta}^{\text{correction}}
\tag{2}
$$

$$
T'_h = \left(\frac{1}{2}\rho W^2 c(c_t\cos\theta + c_n\sin\theta)\right) * \overbrace{\sec\delta}^{\text{correction}}
\tag{3}
$$

Second, normal force is calculated, but radial and vertical components are needed. Normal force is multiplied by the cosine of blade slope to get radial force and multiplied by the sine of blade slope to get vertical force. However, the aforementioned span length must also be included. The resulting reduced equations are shown in Eqs. (4) to (6). F'_R,

F'_T, and F'_Z are the radial, tangential, and vertical force per unit height. No other corrections are required for the blade element equations.

$$F'_R = -c_n \frac{1}{2} \rho W^2 c \tag{4}$$

$$F'_T = \left(c_t \frac{1}{2} \rho W^2 c\right) * \overbrace{\sec\delta}^{correction} \tag{5}$$

$$F'_Z = \left(-c_n \frac{1}{2} \rho W^2 c\right) * \overbrace{\tan\delta}^{correction} \tag{6}$$

3. Verification of Blade-Element Modifications

Figure 4 shows the tangential force of one blade over a revolution of the SNL 5 meter turbine at a tip speed ratio (TSR) of 5.2. The load profile corresponds to approximately 23% of the height (slice 7 of 30). The AC and DMS models were run using stair-stepped vertical slices (cylinders) and the improved formulation including continuous slices with slope as previously described. The AC model is compared in the figure with CACTUS results for the average tangential force along the vertical axis, using CACTUS as the "truth" model. The effect of the local blade slope at this section decreases the general tangential force somewhat and significantly decreases the peaks. The error on the peaks is reduced an order of magnitude and the error on the average force and torque falls from approximately 45% to 3%. Similar trends are seen using DMS.
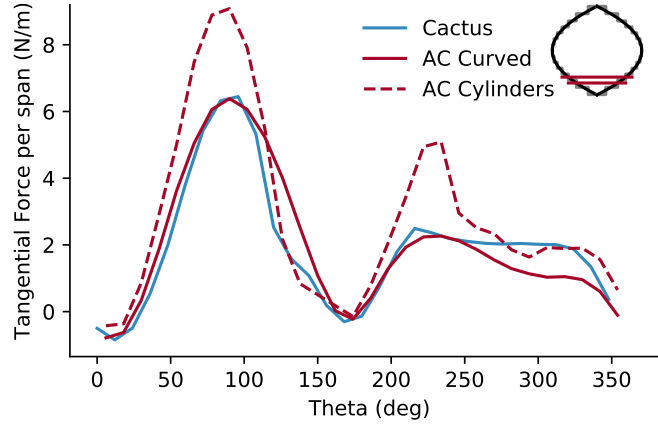

Fig. 4   SNL 5m tangential force comparison between CACTUS and AC at 23% height (slice 7 of 30) shows significant error reduction by including local slope from blade curvature. DMS follows similar trends.

Figure 5 shows both the vertical and radial forces. These forces match well with the mean absolute error for both AC and DMS of less than 1% and a peak force error under 15% for radial and 10% for vertical forces. From these comparisons, can be observed that the vertical induction for this type of turbine may not be as significant as previously concluded.

The effects of the blade slope corrections on the entire turbine's averaged tangential force can be seen in Fig. 6. This measure was chosen to give a 3-D projection of the high level accuracy of the models' blade load predictions, particularly concerning turbine torque performance. Errors approaching 50% can be found around 25% and 75% height, which contribute to an error on the aggregate torque of approximately 14%. Including the sloped blade considerations decreases this to approximately 2%. Similar effects are seen for the full range of TSR and for the other forces. The curved models match much better than the straight over the entire height of the turbine.

4

(a) Steady-state radial force.
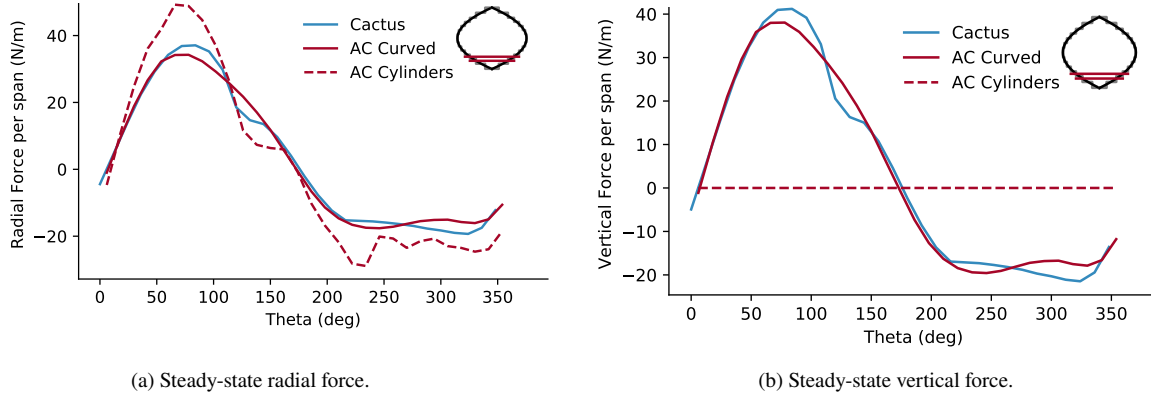
(b) Steady-state vertical force.

Fig. 5 Radial and vertical force comparisons between CACTUS and AC show significant reduction in error by including blade slope including the ability to predict vertical force with a large degrees of accuracy. DMS follows similar trends.
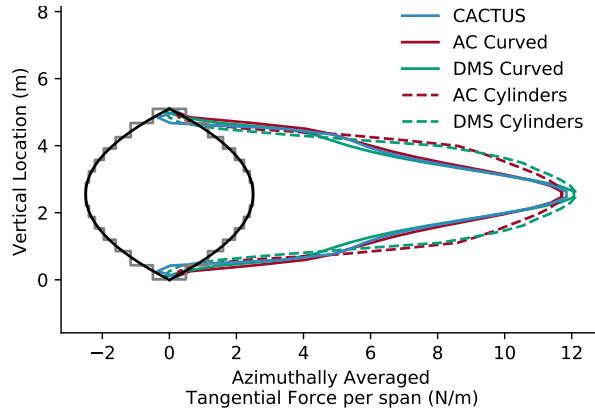

Fig. 6 Average tangential force per span along vertical-axis for SNL 5 meter turbine at TSR of 5.2. Turbine blade shape is in black. Blade slope considerations decrease error compared with the CACTUS 3-D vortex method.

IV. Steady Wake Interaction Modifications

A. Baseline Actuator Cylinder and Double Multiple Streamtube Wake-Turbine Interaction

The AC and DMS methods differ in how the flow field, or wake-induced component is calculated. For DMS, the downstream interaction is approximated by collinear streamtubes where the outlet velocity of the upstream is imposed as the inlet condition on the downstream (see Fig. 7). For DMS, blade slope does not influence this portion of the model. Also, compensating for rotor deformation for DMS is as simple as re-indexing upstream and downstream positions and is not explored here.
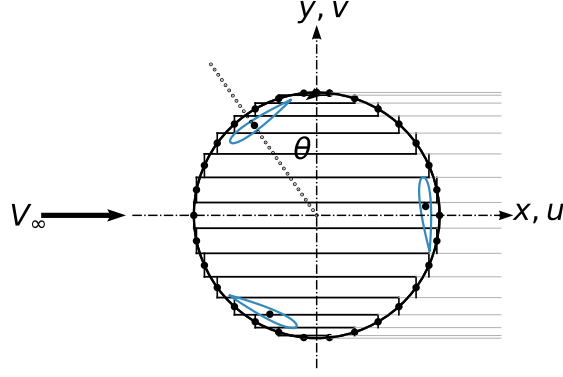
5

Fig. 7 Depiction of DMS streamtubes of constant angular discretization. Aerodynamic coupling one-way with respect to the downstream (light grey tubes) using the upstream (black tubes) exit velocity for a given streamtube.

For the AC method, the downstream interaction is more comprehensive. All azimuthal locations affect one another with what has been termed an *influence coefficient* matrix [12]. This matrix is the influence factor of every position on every other position. Like the blade-element derivations, it was also originally derived for an unchanging radius and straight blades. While a curved deforming blade violates these assumptions, we will show that under most conditions this original formulation may be used with minimal error.

B. Actuator Cylinder Wake-Turbine Influence Coefficient Modifications

The actuator cylinder method commonly used today is actually a linearized version with a nonlinear correction term [7]. By linearizing the method and adding an actuator disk based correction factor [8, 12, 23], significant computational improvements can be made (we use Ning's correction factor, which validates well, but others may be more physically accurate). However, even greater improvements can be made by also reducing the computation required for the intra-turbine influence coefficients. The original formulation did this by assuming an unchanging unit radius and no blade slope. By doing this, the relatively expensive computation associated with integrating each influence term can be done once and reused for any turbine or operating condition with the same azimuthal discretization.

To determine what the influence coefficient matrix should be for a curved deforming blade, we re-derive the linearized equations in 3-D and then reduce them back to a single slice. This is done by starting with the nonlinear actuator surface method [24] and linearizing it using the process for the 2-D AC method as described in Appendix A of Cheng's paper [14]. This process results in the pressure equation shown in Eq. (7), which when integrated for only the terms in parenthesis forms a single influence coefficient.

$$p = \int_0^h \int_0^{2\pi} Q_n \underbrace{\left(r\cos\delta \frac{(-\sin\theta\cos\delta)(x + r\sin\theta) + (\cos\theta\cos\delta)(y - r\cos\theta) + (\sin\delta)(z - z_f)}{\left((x + r\sin\theta)^2 + (y - r\cos\theta)^2 + (z - z_f)^2\right)^{\frac{3}{2}}} \right)}_{\text{influence coefficient}} d\theta dz \tag{7}$$

The position for which the calculation is being performed is x, y, z and the position where the force is generated is depicted by $r\sin\theta$, $r\cos\theta$, and z_f. For a discretized rotor, this double integral is repeatedly integrated for each blade position's influence on all other needed positions, thus forming an influence coefficient matrix. The actuator cylinder normal volume force Q_n is as described by Cheng and others but is corrected for blade slope as described previously. Using this equation, if one assumes a unit radius, zero blade slope, and unit height (2-D representation) then all of the r, $\cos(\delta)$ and z terms drop out. The $\frac{3}{2}$ bottom exponent goes to $\frac{2}{2}$ or 1 because integration by parts is now done for 2 dimensions instead of 3. The equation then becomes the original infinite-cylinder and unchanging radius equation as described in the literature.

For our purposes, we are interested in calculating forces for a curved and deforming blade but maintain the 2-D simplicity and speed. We therefore only drop the z terms and the bottom exponent as described above. Since the coefficient is non-dimensional and we will be using a different radius for each azimuthal angle, each radius value is normalized by the mean radius of the turbine slice of interest. The downside this approach is that though the influence

coefficient matrix is still independent of absolute radius, it must be recalculated every time there is a change in the normalized radius vector or blade slope.

C. Sensitivity of Actuator Cylinder Influence Coefficient Modifications

To show the relative effect of varying radius, we define a test case based on a circular path with increasing ovality. This is done using the SNL 5 meter turbine at the constant rotation rate and inflow velocity used previously for the 5.2 TSR case. Additionally, we look at a slice at the equator to decouple from blade slope. We keep the mean radius of the oval at the nominal turbine radius, but increase the ovality from 0-100%. Percent ovality is defined as percent elongation of radius along the major axis, with the minor axis radius scaled such that the mean radius equals the nominal radius. We present the worst case of alignment, which is approximately 45 degrees. The resulting path is shown in Fig. 8a. Figure 8b shows the solution with the influence coefficient modifications is shown with dashed lines, while the standard uncorrected approach is shown with straight lines. Both types include the varying radius in the blade element equations, but only the modified case has the varying radius effects in the influence coefficient matrix. Similar levels of difference were seen for the vertical and radial forces. The worst case root mean square error is 0.86 (2.8% of the max absolute value) and occurs with 100% ovality. Error at the peak negative load is 7.7% at approximately 45 degrees azimuth. Error at the peak positive load is 1.5% at approximately 100 degrees azimuth.

(a) Blade path for varying ovality.

(b) Tangential force for varying ovality. Dahsed lines include influence coefficient modification, straight lines do not.
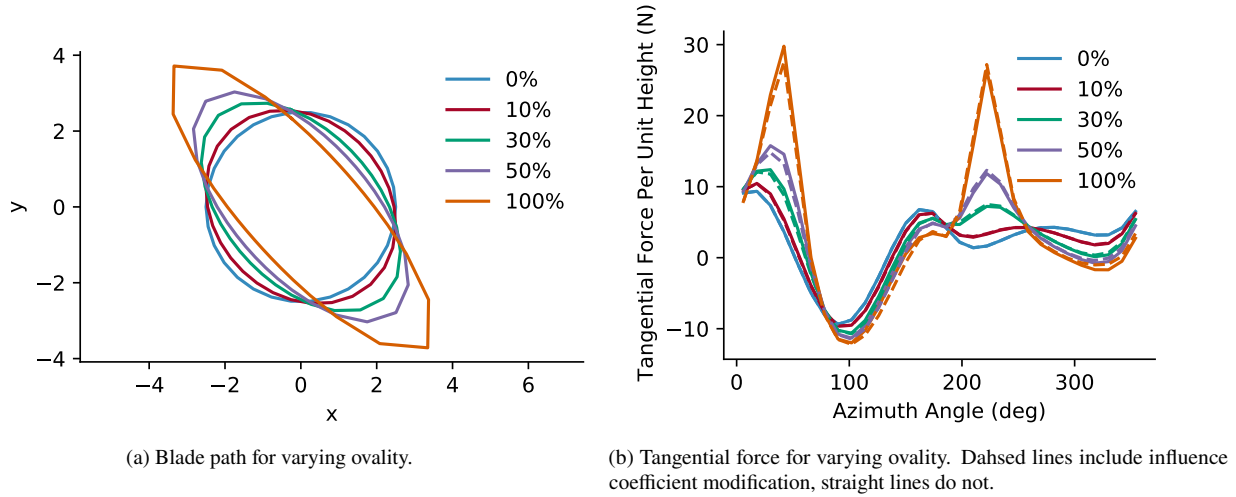
Fig. 8   Effect of capturing varying radius in the actuator cylinder influence coefficient matrix. Maximum root mean square error is 0.86 N for 100% ovality.

Based on this analysis and the minor relative difference, one might neglect the varying radius interaction in the influence coefficient matrix. One might also neglect this effect during an exploratory phase where the speed associated with a constant influence coefficient matrix is needed. The speed difference of precomputing the influence coefficient matrix can be as much as 7x faster depending on operating conditions, but most cases we ran gave a 2-3x speedup.

To show the relative effect of varying blade slope on the influence coefficients, we use the same SNL 5m turbine at a TSR of 5.2. This turbine naturally has a blade slope ranging from approximately 0-60 degrees. As before, the blade slope vector is included in the blade element equations, but only the modified version includes blade slope in the influence coefficients. Figure 9a shows the resulting revolution-averaged tangential forces and Fig. 9b shows the percent difference. The difference in tangential force becomes significant as the slope increases towards 60 degrees. However, its effect on the local torque produced is minimal, staying below 4%. Similar levels of difference were seen for the radial and vertical forces. Therefore, similar to a varying radius, it seems that neglecting this effect entirely would be reasonable for this type of turbine. However, turbines with large or actively changing blade slope in areas that contribute significantly to forces may need this modification. This may be the case for a V-VAWT or H-VAWT with tilted blades. Computational speed differences between precomputing or including this effect are the same as for the varying radius effects and the two modifications should be used together if used.

(a) Tangential force comparing slope in the AC influence coefficients.

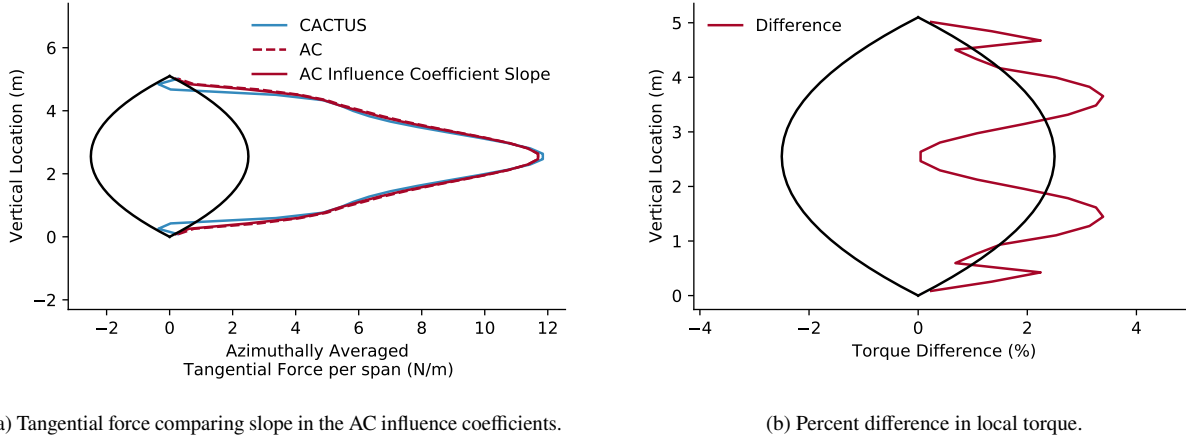(b) Percent difference in local torque.

Fig. 9   Effect of capturing varying slope in the actuator cylinder influence coefficient matrix is minimal for both tangential force and the resulting torque. Similar differences were seen for the radial and vertical forces.

V. Unsteady Theory Modifications

A. Unsteady Approximation Baseline

The DMS and AC base models are steady-state, but calculations are done at each azimuthal location for an entire revolution. This revolution would match the last revolution of an unsteady simulation that has achieved steady-state. Additionally, if parameters and conditions associated with each azimuthal discrete point around the turbine are used, time-varying inputs can be included in the calculations. Examples include varying blade shape, inflow conditions, and rotational speed. If these azimuthally varying inputs are repeatedly used (for each revolution) in conjunction with a high-pass first-order filter on the induced velocities, as done by Larsen [25], an unsteady time-domain approximation can be made. New induced velocities are calculated and combined with old through the filter, then unsteady performance is determined from the resulting filtered induced velocities that are re-run through the models. Like full unsteady models, this models transient behavior until steady-state is achieved after multiple revolutions. This is similar to the method used for horizontal-axis wind turbine (HAWT) blade element momentum theory [26] and has been used in the VAWT adaptations of HAWC2 [8, 25], SIMO-RIFLEX-AC [9], and a TU Delft study [10]. However, the method requires all azimuthal values be re-calculated at each timestep, even though the theoretical blades are not present at all positions.

B. Rotating Point Iterative (RPI) Solution Method

Our intended use for DMS and AC is for system design and optimization within a fully coupled aero-hydro-servo-elastic analysis tool. This type of coupled analysis in the time domain can become computationally expensive very quickly. Removing unnecessary aerodynamic calculations by only solving the AC or DMS methods for the current blade positions would give a significant advantage for analysis and design. To accomplish this requires a rotating index of azimuthal positions to be solved. As the simulation progresses, a given point on the circumference of the blade path would appear to be iterated on, similar to a fixed point iterative method. Therefore, we characterize this method as a rotating point iterative (RPI) method. There are four key modifications required to the base steady and unsteady models to achieve an accurate unsteady approximation with RPI.

First, the base AC and DMS solution methods need to be modified. Adjacent streamtubes are not coupled in DMS and downstream tubes only need the upstream's exit velocity. Therefore, one must simply keep a history of azimuthal values/calculations and re-solve each streamtube indicated by the rotating index, using the historical upstream values as necessary. For AC, this must also be done, but additionally requires an invasive modification to the solution methodology. AC solves using the co-influence of every position on every other position, which creates a square nonlinear solution matrix (same number of inputs as outputs). RPI needs the solution to just the current blade positions, keeping all else constant, but the co-influence calculations remain. This creates a non-square nonlinear solution matrix (less inputs than outputs) requiring a special solver, such as Levenberg-Marquardt [27]) to be used.

Second, all time-varying values except inflow velocity can be updated with the rotating index as they become available (e.g. aerostructural blade deformation and rotational rate which are known only at the blade positions). The

inflow velocity must be updated at every azimuthal position at every timestep since the induced velocities are dependent on inflow velocity. Updating inflow velocity at only the rotating index causes significant error for unsteady inflow conditions like gusts and turbulence.

Third, the rotating index resets once it begins to overlap the next blade's starting point; continuing in an overlapped state is not necessary. One simply tracks the theoretical blade positions normally regardless of which rotating index corresponds to which blade.

Fourth, the fixed point iteration at each azimuthal point numerically converges after about 2 iterations (two blade passes), which influences the high-pass filtering of the unsteady method. The time constants of the filter as described by [25], should be tuned against a higher order method for the specific turbine type and number of blades (we used 3 blades which resulted in near and far wake time constants of 0.3 and 3.0 when tuned against CACTUS).

1. RPI Algorithmic Implementation

Algorithm 1 gives an in-depth look at how the RPI method is implemented. For completeness, the algorithm shows how the modifications fit into the first order filter (Line 38). It also shows how to resolve timesteps that cause rotations smaller than the azimuthal discretization as can be common if coupled to unsteady structural dynamics (Line 43). It should also be noted that the algorithm shown assumes Fortran-like one-based indexing.

Algorithm 1 Rotating Point Iterative (RPI) Solution Method

1: **Initialize scalars and integers:**
2: Tol # convergence tolerance
3: N_θ # number of azimuthal discretizations
4: $\text{step}_{\text{last}}$ # index of last timestep
5: V_{wakeOld} # average wake velocity at last timestep
6: B # number of blades
7: R_{ref} # reference radius
8: ρ # air density
9: dt # timestep
10: t_{max} # total time
11: τ_{near} # near wake time constant
12: τ_{far} # far wake time constant
13: **Initialize arrays and matrices:**
14: ω # rotation rate
15: r # radius
16: β # blade twist
17: δ # blade slope
18: $V_{\text{inf Local}}$ # local freestream velocity
19: w_{old} # stacked array of induced velocities for u and v for last timestep
20: cl, cd $\leftarrow$ getAirfoilPolars
21: $A \leftarrow$ getInfluenceCoefficients(N_θ) #If DMS, A is not used
22: **for** $t \leftarrow 0 : dt : t_{\text{max}}$ **do**
23:     $w \leftarrow w_{\text{old}}$
24:     $\theta, \omega_{\text{RPI}}, r_{\text{RPI}}, \beta_{\text{RPI}}, \delta_{\text{RPI}}, V_{\text{inf ALL}}, V_{\text{deflections}} \leftarrow$ rotorState (i.e. deformation, dynamics, inflow)
25:     $\text{step} \leftarrow \text{ceiling}\left(\frac{\theta}{2\pi/N_\theta}\right)$
26:     $\text{step}_{\text{circular}} \leftarrow \text{step} - floor\left(\frac{\text{step}-1}{N_\theta B}\right)\frac{N_\theta}{B}$
27:     $\text{idx}_{\text{RPI}} \leftarrow \left(\text{step}_{\text{circular}}\right) : \left(\frac{N_\theta}{B}\right) : \left(2N_\theta - \frac{N_\theta}{B} + 1 + \text{step}_{\text{circular}}\right)$
28:     $\omega(\text{idx}_{\text{RPI}}) \leftarrow \omega_{\text{RPI}}$
29:     $r(\text{idx}_{\text{RPI}}) \leftarrow r_{\text{RPI}}$
30:     $\beta(\text{idx}_{\text{RPI}}) \leftarrow \beta_{\text{RPI}}$
31:     $\delta(\text{idx}_{\text{RPI}}) \leftarrow \delta_{\text{RPI}}$
32:     $V_{\text{inf Local}} \leftarrow V_{\text{inf ALL}}$
33:     **while** residual($w, \omega, r, \beta, \delta, V_{\text{inf Local}}, B, \rho,$ cl, cd, $V_{\text{deflections}}, A$) > Tol **do**
34:         $w(\text{idx}_{\text{RPI}}) \leftarrow$ root solver
35:     **end while**
36:     # Get average turbine induction in the freestream direction a
37:     $[\sim, \sim, \sim, a_{\text{new}}] \leftarrow$ turbinePerformance($w, \omega, r, \beta, \delta, V_{\text{inf Local}}, B, \rho,$ cl, cd, $V_{\text{deflections}}$)
38:     $\tau_1 \leftarrow \tau_{\text{near}} R_{\text{ref}}/V_{\text{wakeOld}}$
39:     $\tau_2 \leftarrow \tau_{\text{far}} R_{\text{ref}}/V_{\text{wakeOld}}$
40:     $w_{\text{filtered}} \leftarrow w_{\text{old}}e^{-dt/\tau_1} + w(1 - e^{-dt/\tau_1})$
41:     $V_{\text{wakeFiltered}} \leftarrow V_{\text{wakeOld}}e^{-dt/\tau_2} + \overline{V_{\text{inf Local}}}(1 - 2a_{\text{new}})(1 - e^{-dt/\tau_2})$ # use average local velocity
42:     $[F_R'(\theta), F_T'(\theta), F_Z'(\theta), \sim] \leftarrow$ turbinePerformance($w_{\text{filtered}}, \omega, r, \beta, \delta, V_{\text{inf Local}}, B, \rho,$ cl, cd, $V_{\text{deflections}}$)
43:     **if** $\text{step}_{\text{last}} \neq \text{step}$ **then**
44:         $w_{\text{old}} \leftarrow w_{\text{filtered}}$
45:         $V_{\text{wakeOld}} \leftarrow V_{\text{wakeFiltered}}$
46:         $\text{step}_{\text{last}} \leftarrow \text{step}$
47:     **end if**
48: **end for**

C. Adaptations for Turbulent Inflow

Turbulent inflow calculations generally include cross-flow and up-flow, which requires an update to the models' inflow velocity equations. For simplicity, we term V_∞ from Eq. (1) as V_x and term cross-flow V_y and up-flow V_z using the standard coordinate system. Re-deriving the normal and tangential velocity components including these additional velocity components and their influence on the planar induced velocities calculated by AC and DMS gives the equations shown in Eq. (8). For DMS, no cross-flow induction is calculated, so all v terms go to zero.

$$
\begin{aligned}
V_n &= \left(V_x(1+u)\sin\theta - V_x(v)\cos\theta - V_y(1+v)\cos\theta + V_y(u)\sin\theta\right) * \cos\delta \;\; + \;\; V_z * \sin\delta \\
V_t &= \; V_x(1+u)\cos\theta + V_x(v)\sin\theta + \; V_y(1+v)\sin\theta + V_y(u)\cos\theta + \Omega r
\end{aligned}
\tag{8}
$$

D. Unsteady Method Verification

VAWTs differ from HAWTs in that they have non-negligible depth in the freestream direction. This makes modeling turbulent transport [28] necessary for VAWTs. As a gust passes through the turbine, different sections of the turbine encounter different freestream speeds. A rotating blade can go in and out of the gust as it passes. For example, in Fig. 10 we compare the freestream velocity of a gust as seen at the hub versus the freestream velocity seen by blade 1 as it moves up and down stream (blade 1 starts at 0 azimuth angle per Fig. 1, 36 timesteps per revolution). The base simulation used matches the SNL 5 meter 5.2 TSR simulations as previously described. The gust velocity used is 5 m/s and a duration of 0.8 seconds corresponding to approximately one revolution. This time-changing velocity distribution must be correctly mapped to the numerical vectors corresponding with each azimuthal location for AC and DMS to ensure turbulent transport is included correctly.
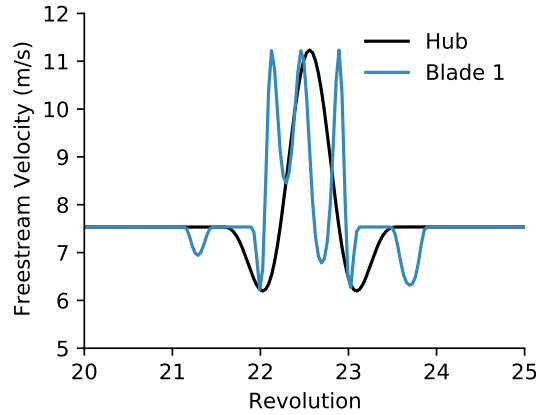

Fig. 10   Freestream velocity at the hub and at blade 1 (as it moves) during large gust passage at 23% height or slice 7 of 30.

Applying the gust defined above including turbulent transport, we compare the AC, DMS and CACTUS models. Figure 11 shows the baseline CACTUS response in tangential force for the specified blade position. Referring back to Fig. 10, the gust is centered at revolution 22.75, and has multiple rapid increases and decreases in velocity seen by the passing blade. In Fig. 11 at revolution 20, the loads are periodic steady-state. At revolution 21, there is a slight decrease in the peak force as the blades start to dip into the gust on the upstream, or high torque side. At revolution 22, most of the turbine is in the gust and the high torque side increases and widens. Then, associated with a sharp decrease-increase-decrease in velocity on the downstream, or low torque side, the force spikes just before revolution 23. After revolution 23, the forces tend to return to periodic steady-state. There are several key takeaways here:

- The RPI method is nearly identical (less than 1% difference) to the original 1st order filter method for all cases while being numerically more efficient.
- The reduced order methods capture much of the load profile and variation, but not all.
- The DMS method gives similar results as AC, but under-predicts the secondary downstream loads.
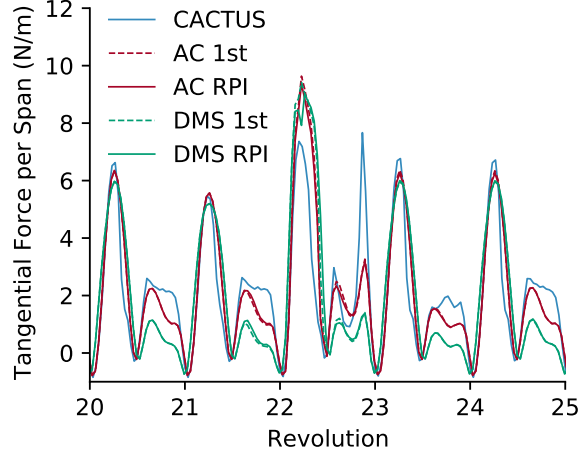
Fig. 11 **Tangential force for blade 1 at 23% height (slice 7 of 30). RPI and original 1st order filter methods differ by less than 1%.**

The trends for the radial and vertical forces are similar to the tangential force as seen in Fig. 12. Though not shown, these similar trends also are exhibited for the other two blades and as blade slope increases towards the top of the turbine.
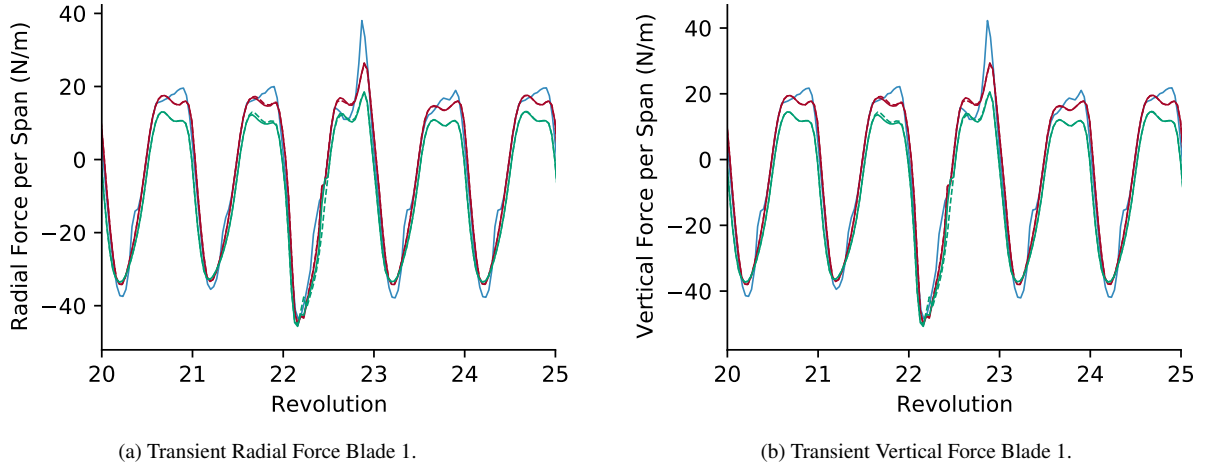

(a) Transient Radial Force Blade 1.

(b) Transient Vertical Force Blade 1.

Fig. 12 **Radial and vertical force at 23% height (slice 7 of 30). RPI and original 1st order filter methods differ by less than 1%. Plot colors match Fig. 11.**

E. Numerical Efficiency

To quantify the numerical efficiency of the RPI method, we run time tests with an i7 3.1GHz processor limited to 1 thread. The CACTUS solver is fortran and is locally compiled per the user instructions. Both AC and DMS are implemented in the Julia language, version 1.5 [29]. The comparison case is the gust case detailed above with 36 azimuthal discretizations. For a best case timing scenario, and because dynamic stall is not active at these conditions, the dynamic stall model was turned off for all models. (Dynamic stall adds about a 1.5x penalty on average but some AC cases can see as much as a 7x penalty). The AC influence coefficient modifications were also turned off and the faster precomputation method used. All unsteady simulations were run for 40 revolutions, which results in a real time turbine at 150 rpm spinning at 0.4 seconds/revolution.

Table 1 Computational speed comparison between the original unsteady approximation and the RPI modification. CACTUS and realtime speeds also listed for reference. RPI produces a 5-10x speedup over the original formulation. DMS running RPI runs over 5000x faster than CACTUS and 27% faster than realtime.

	Original 1st Order Filter	RPI
Actuator Cylinder	1.05 min/rev	5x faster (12.53 s/rev)
Double Multiple Streamtube	2.93 s/rev	10x faster (0.29 s/rev)
CACTUS Reference	25.5 min/rev	
Realtime Turbine Reference	0.4 s/rev	

Table 1 summarizes the relative performance for full 3-D unsteady simulation. The ideal difference in RPI solution speed versus the original 1st order filter is 12x (36 azimuthal discretizations divided by 3 blades), but computational overhead reduces this. The DMS method has little overhead because it uses simple coupling and a 1D superlinear root finder used for its residual equation, resulting in a 10x speedup. The AC method's intra-turbine coupling and n-dimensional root solver generate higher levels of overhead, resulting in only a 5x speedup. A one-to-one comparison puts DMS with RPI at about 5275x faster than CACTUS, and about 27% faster than realtime. Computational speed is based on azimuthal discretization and larger turbines spin slower, so a larger turbine modeled using the same discretization would give an even better relative performance to realtime. These models are highly parallelizable, and could be sped up even more to enable applications like real-time unsteady predictive control.

VI. Conclusions and Future Work

The motivation of this study was to improve the actuator cylinder (AC) and double multiple streamtube (DMS) models to enable faster and more accurate floating system design. We removed the majority of the error for curved blades associated with the original straight-blade assumption by modifying the blade-element equations to include the true blade-normal frame of reference. We also addressed the intra-turbine coupling assumptions, re-deriving the AC influence coefficient matrix. We found that for the majority of standard Darrieus turbine shapes and operation, one can neglect the intra-turbine effects varying radius and blade slope cause and use the faster precomputation method with only modifications in the blade element equations. Finally, we showed how to include unsteady inputs in the steady state AC and DMS models, and gave a new rotating point iterative (RPI) method for solving the unsteady equations with 5-10x reduced computation time and negligible change in predicted forces (<1%).

Our results show that these simple AC and DMS models can now predict loads nearly as well as higher order 3-D vortex methods such as CACTUS, but with orders of magnitude greater speed. The AC method running RPI is 122x faster than CACTUS with comparable loads accuracy. DMS running RPI is 5275x faster than CACTUS with comparable accuracy. By coupling to a structural code such as OWENS [30] we can explore full aero-elastic turbine design with CACTUS-comparable accuracy, but as much as 5000x faster.

Acknowledgments

References

[1] Templin, R., "Aerodynamic performance theory for the NRC vertical-axis wind turbine," *NASA STI/RECON technical report n*, Vol. 76, 1974. OSTI Report Number(s): N-76-16618; LTR-LA-160.

[2] Wilson, R. E., and Lissaman, P. B., "Applied aerodynamics of wind power machines," *National Science Foundation*, 1974. OSTI Report Number(s): NSF/RA/N-74-113.

[3] Strickland, J., "A performance prediction model for the darrieus turbine," *International symposium on wind energy systems*, 1977, pp. C3–39.

[4] Paraschivoiu, I., "Double-multiple streamtube model for studying vertical-axis wind turbines," *Journal of Propulsion and Power*, Vol. 4, No. 4, 1988, pp. 370–377. https://doi.org/10.2514/3.23076, URL https://doi.org/10.2514/3.23076.

[5] Paraschivoiu, I., and Delclaux, F., "Double multiple streamtube model with recent improvements (for predicting aerodynamic loads and performance of Darrieus vertical axis wind turbines)," *Journal of Energy*, Vol. 7, No. 3, 1983, pp. 250–255. https://doi.org/10.2514/3.48077, URL https://doi.org/10.2514/3.48077.

[6] Ayati, A. A., Steiros, K., Miller, M. A., Duvvuri, S., and Hultmark, M., "A double-multiple streamtube model for vertical axis wind turbines of arbitrary rotor loading," *Wind Energy Science*, Vol. 4, No. 4, 2019, pp. 653–662. https://doi.org/10.5194/wes-4-653-2019, URL https://wes.copernicus.org/articles/4/653/2019/.

[7] Madsen, H., "The Actuator Cylinder - A Flow Model for Vertical Axis Wind Turbines," Thesis, Technical University of Denmark, 01 1982. https://doi.org/10.13140/RG.2.1.2512.3040.

[8] Madsen, H., Larsen, T., Vita, L., and Paulsen, U., "Implementation of the Actuator Cylinder flow model in the HAWC2 code for aeroelastic simulations on Vertical Axis Wind Turbines," *51st AIAA Aerospace Sciences Meeting including the New Horizons Forum and Aerospace Exposition*, 2013. https://doi.org/10.2514/6.2013-913, URL https://arc.aiaa.org/doi/abs/10.2514/6.2013-913.

[9] Cheng, Z., Madsen, H. A., Gao, Z., and Moan, T., "A fully coupled method for numerical modeling and dynamic analysis of floating vertical axis wind turbines," *Renewable Energy*, Vol. 107, 2017, pp. 604 – 619. https://doi.org/https://doi.org/10.1016/j.renene.2017.02.028, URL http://www.sciencedirect.com/science/article/pii/S0960148117301143.

[10] Koppenol, B. S., "Dynamic Analysis of a Floating Vertical Axis Wind Turbine using the Actuator Cylinder Flow Theory - Comparative study on a land-based versus spar vertical axis wind turbine concept and a code-to-code comparison," Thesis, Delft University of Technology, 09 2016. https://doi.org/uuid:24ecd297-323e-4b75-9f76-6b10c337681a.

[11] Ferreira, C. S., Madsen, H. A., Barone, M., Roscher, B., Deglaire, P., and Arduin, I., "Comparison of aerodynamic models for Vertical Axis Wind Turbines," *Journal of Physics: Conference Series*, Vol. 524, 2014, p. 012125. https://doi.org/10.1088/1742-6596/524/1/012125, URL https://doi.org/10.1088%2F1742-6596%2F524%2F1%2F012125.

[12] Ning, A., "Actuator cylinder theory for multiple vertical axis wind turbines," *Wind Energy Science*, Vol. 1, No. 2, 2016, pp. 327–340. https://doi.org/10.5194/wes-1-327-2016, URL https://wes.copernicus.org/articles/1/327/2016/.

[13] Tavernier, D. D., Sakib, M., Griffith, T., Pirrung, G., Paulsen, U., Madsen, H., Keijer, W., and Ferreira, C., "Comparison of 3D aerodynamic models for vertical-axis wind turbines: H-rotor and Φ-rotor," *Journal of Physics: Conference Series*, Vol. 1618, 2020, p. 052041. https://doi.org/10.1088/1742-6596/1618/5/052041, URL https://doi.org/10.1088%2F1742-6596%2F1618%2F5%2F052041.

[14] Cheng, Z., Madsen, H. A., Gao, Z., and Moan, T., "Aerodynamic Modeling of Floating Vertical Axis Wind Turbines Using the Actuator Cylinder Flow Method," *Energy Procedia*, Vol. 94, 2016, pp. 531 – 543. https://doi.org/https://doi.org/10.1016/j.egypro.2016.09.232, URL http://www.sciencedirect.com/science/article/pii/S1876610216309195, 13th Deep Sea Offshore Wind R&D Conference, EERA DeepWind'2016.

[15] Wang, K., Hansen, M., and Moan, T., "Model improvements for evaluating the effect of tower tilting on the aerodynamics of a vertical axis wind turbine," *Wind Energy*, Vol. 18, 2014, pp. 91–110. https://doi.org/10.1002/we.1685.

[16] Leroy, V., "Unsteady aerodynamic modelling for seakeeping analysis of Floating Offshore Wind Turbines," Theses, École centrale de Nantes, Dec. 2018. URL https://tel.archives-ouvertes.fr/tel-02090543.

[17] Sheldahl, R. E., and Blackwell, B. F., "Free-Air Performance Tests of a 5-Metre-Diameter Darrieus Turbine," Tech. Rep. SAND-77-1063, Sandia National Laboratories, 12 1977.

[18] Sheldahl, R. E., Klimas, P. C., and Feltz, L. V., "Aerodynamic Performance of a 5-Metre-Diameter Darrieus Turbine With Extruded Aluminum NACA-0015 Blades," Tech. Rep. SAND-80-0179, Sandia National Laboratories, 3 1980.

[19] Murray, J., and Barone, M., "The Development of CACTUS, a Wind and Marine Turbine Performance Simulation Code," *49th AIAA Aerospace Sciences Meeting including the New Horizons Forum and Aerospace Exposition*, 2012. https://doi.org/10.2514/6.2011-147, URL https://arc.aiaa.org/doi/abs/10.2514/6.2011-147.

[20] Klimas, P. C., and Worstell, M. H., "Effects of blade preset pitch/offset on curved-blade Darrieus vertical axis wind turbine performance," 1981. SAND-81-1762.

[21] Tarzanin, F., "Prediction of control loads due to blade stall," *Journal of the American Helicopter Society*, Vol. 17, No. 2, 1972, pp. 33–46. https://doi.org/https://doi.org/10.4050/JAHS.17.33.

[22] Glauert, H., *The Elements of Aerofoil and Airscrew Theory*, Cambridge Science Classics, Cambridge University Press, 1983. https://doi.org/10.1017/CBO9780511574481.

[23] Steiros, K., and Hultmark, M., "Drag on flat plates of arbitrary porosity," *Journal of Fluid Mechanics*, Vol. 853, 2018, p. R3. https://doi.org/10.1017/jfm.2018.621.

[24] Madsen, H., "Application of Actuator Surface Theory on Wind Turbines," Technical University of Denmark, 1988.

[25] Larsen, T., and Aagaard Madsen, H., "On the way to reliable aeroelastic load simulation on VAWT's," 2013. URL http://www.ewea.org/annual2013/, european Wind Energy Conference ; Exhibition 2013, EWEA 2013 ; Conference date: 04-02-2013 Through 07-02-2013.

[26] Sørensen, N., Aa, H., and Madsen, H., "Modelling of transient wind turbine loads during pitch motion," *European Wind Energy Conference and Exhibition 2006, EWEC 2006*, Vol. 1, 2006.

[27] Moré, J. J., "The Levenberg-Marquardt algorithm: implementation and theory," *Numerical analysis*, Springer, 1978, pp. 105–116. URL https://www.osti.gov/servlets/purl/7256021/.

[28] Taylor, G. I., "The Spectrum of Turbulence," *Proceedings of the Royal Society A: Mathematical, Physical and Engineering Sciences*, Vol. 164, No. 919, 1938, pp. 476–490. https://doi.org/10.1098/rspa.1938.0032, URL https://royalsocietypublishing.org/doi/abs/10.1098/rspa.1938.0032.

[29] Bezanson, J., Edelman, A., Karpinski, S., and Shah, V. B., "Julia: A fresh approach to numerical computing," *SIAM review*, Vol. 59, No. 1, 2017, pp. 65–98. URL https://doi.org/10.1137/141000671.

[30] Owens, B. C., "Theoretical Developments and Practical Aspects of Dynamic Systems in Wind Energy Applications," Ph.D. thesis, Texas A & M University, 2013. URL http://hdl.handle.net/1969.1/151813.